Alcántara-Ávila, F.; Hoyas, S.; Pérez Quiles, MJ. (2018). DNS of thermal channel flow up to Re-tau=2000 for medium to low Prandtl numbers. International Journal of Heat and Mass Transfer. 127:349-361. https://doi.org/10.1016/j.ijheatmasstransfer.2018.06.149

DNS of thermal channel flow up to $Re_\tau = 2000$ for medium to low Prandtl numbers

F. Alcántara-Ávila[a], S. Hoyas[a,*], M.J. Pérez-Quiles[a]

[a] *Instituto Universitario de Matemática Pura y Aplicada, Universitat Politècnica de València, Valencia 46022, Spain.*

Abstract

Direct Numerical Simulations of turbulent heat transfer in a channel flow are presented for three different Reynolds numbers, namely $Re_\tau = 500$, 1000 and 2000. Medium and low values of the molecular Prandtl number are studied, ranging from 0.71 (air), down to 0.007 (molten metals), in order to study its effect on the thermal flow. Mixed boundary conditions at both walls are used for the thermal flow. Mean value and intensities of the thermal field were obtained. Two different behaviors were observed, depending on the Prandtl and Péclet numbers. The expected logarithmic behavior of the thermal flow completely disappears for Prandtl below 0.3. This is a direct effect of the thicker viscous thermal layer generated as the Prandtl number is reduced. Von Kármán constant was computed for cases above this Prandtl, and turbulent Prandtl and Nusselt numbers were obtained for all the cases. Finally, the turbulent budgets for heat fluxes, temperature variance and its dissipation rate are presented. As a general result, there is a scaling failure near the wall in very cases studied, which is accentuated for lower Prandtl numbers. The statistics of all simulations can be downloaded from the web page of our `group`.

Keywords: Turbulent channel flow, Heat transfer, Prandtl number, Péclet number, Scaling law

List of symbols

B	Logarithmic profile constant
c_p	Specific heat at constant pressure
h	Channel half height
$\mathfrak{h}$	Convective heat transfer coefficient
Nu	Nusselt number
P	Pressure
Pe_τ	Péclet number ($=Re_\tau Pr$)
Pr	Prandtl number ($=\nu/\alpha$)
$\mathrm{Pr_t}$	Turbulent Prandtl number
q_w	Normal heat flux to the walls
q_{total}	Total heat flux
Re	Reynolds number ($=U_b h/\nu$)
Re_τ	Reynolds friction number ($=u_\tau h/\nu$)
t	Time
T_τ	Friction temperature $\left(=q_w/\left(\rho c_p u_\tau\right)\right)$
u_i	Velocity fluctuation
u_τ	Friction velocity $\left(=\sqrt{\tau_w/\rho}\right)$
U_i	Velocity in the direction x_i
U_b	Bulk velocity $\left(=\langle U_1\rangle_{x,y,z,t}\right)$
x_i	Coordinate x_i ($\equiv x, y, z$)

*Corresponding author. e-mail: serhocal@mot.upv.es. Tel: +34 - 96 38 77007 (ext 76563)

Greek

α	Thermal diffusion coefficient
θ	Temperature fluctuation
Θ	Transformed temperature
κ	Thermal conductivity
κ_t	Thermal von Kármám constant or thermal eddy diffusivity
ν	Viscosity
ν_t	Momentum eddy diffusivity
ρ	Density
τ_w	Statistically averaged wall shear stress

Superscripts

$\bullet'$	Root mean square
$\overline{\bullet}$	Statistically averaged
$\bullet$	Normalized by h, U_b and ν
$\bullet^+$	Normalized by u_τ, T_τ and ν

Subscripts

$\langle\bullet\rangle_{x_i}$	Mean value in x_i direction

1. Introduction

Turbulent flows are intrinsic to almost any flow in engineering. Particularly, they play a crucial role in the transport of heat. In a recent study for NASA, Slotnick et al [1] highlighted the importance of thermal flows in aeronautics applications for the foreseeable future. As an example, the performance of the high pressure turbines present in aircraft engines is limited by the maximum temperature that can be reached without deforming the blades. An improvement in the knowledge of thermal flow around the blade could then increase the efficiency and reduce the emissions of the engine [2], [3]. To cite only a couple of examples, for low and very low Prandtl numbers a better knowledge of the dynamics of thermal flows is needed for the simulation of nuclear Liquid Metal Reactors (LMR) [4, 5]. Also, a direct application of the very low Prandtl cases is concentrated solar power (CSP), as stated in Cachafeiro et al. [6]. However, the dynamics of turbulent flows is still an open problem in physics. If thermal flows are included, the situation is even worse, due to the complexity of thermal flows experiments. Thus, Direct Numerical Simulation (DNS) has become one of the main tools to study the behaviour of thermal flows where little is known.

The first DNS of a thermal flow was carried out by Kim and Moin in 1987 [7], for $Re_\tau = u_\tau h/\nu \approx 180$ and $Pr = 0.1$, 0.71 and 2, where u_τ is the friction velocity, h is the half channel height and ν is the kinematic viscosity. The friction Reynolds number, Re_τ, characterize the turbulent behaviour of the flow. The molecular Prandtl number, Pr, is the ratio between the momentum diffusivity (kinematic viscosity) to the thermal diffusivity. In this work, values from 0.007 (melted sodium) to 0.71 (air) are studied. Another dimensionless number that can be derived from Re_τ and Pr is the friction Péclet number, $Pe_\tau = Re_\tau Pr$. Pe_τ plays the same role in the thermal equation than Re_τ does in the momentum equations. Therefore, Pe_τ can be understood as a parameter of how viscous or turbulent the thermal flow is.

Kim and Moin [7] obtained first order turbulence statistics, including the turbulent Prandtl number, defined later. In addition, for $Pr = 0.71$, correlations between the velocity and the temperature were also calculated. A somewhat artificial boundary condition was imposed in which heat was generated internally and removed from both cold isothermal walls. This condition for the thermal flow plays an analogous role to that of the pressure gradient does for the velocity field. Later, Lyons et al. [8] performed a simulation for $Re_\tau \approx 150$ and $Pr = 1$. The boundary condition used in this later work consisted in both walls kept at different temperatures. Finally, Kasagi et al. [9] performed a DNS for $Re_\tau \approx 150$ and $Pr = 0.71$ with a more realistic boundary condition, the Mixed Boundary Condition (MBC from now on). For this condition, the average heat flux over both heating walls is constant and the temperature increases linearly in the streamwise direction. The instantaneous heat flux may vary with respect to time and position. This is the boundary condition used in this work.

In the work done by Piller [10], three different boundary conditions were used and the differences in the temperature field were studied. The first one, ideal isoflux boundary condition, assumes that the instantaneous wall heat fux is both uniform in space and constant in time. Therefore, the tieme-averaged temperature is linear with x. For the ideal isothermal boundary condition, the time-averaged wall temperature is uniform and constant, resulting in an exponential variation of the time-averaged temperature difference. The last one was the MBC, the one used in this work (explained above). He found that the MBC acts as an ideal isothermal boundary condition in the inner layer and as an ideal isoflux boundary condition in the outer layer.

After these simulations were made, the trend has been to increase the friction Reynolds number for different molecular Prandtl numbers. However, values of Re_τ and Pr are limited by the computational cost, which can be approximated by $L_x^2 L_y Re_\tau^4 Pr^{3/2}$ [11]. Thus, the Reynolds number achieved is still low for a majority of Prandtl numbers. Kawamura et al. [12] made an exhaustive analysis of the Prandtl number influence for $Re_\tau \approx 180$. Pr varied for a wide range from 0.025 to

5. First order turbulent statistics were calculated, but also the budgets of the transport equations for the turbulent heat flux and the temperature variances were obtained. One year later, Kawamura et al. [13] performed a new simulation increasing the Reynolds number up to a value of $Re_\tau \approx 395$ and for $Pr = 0.025$, 0.2 and 0.71. They obtained the same set of results than in the previous paper and also images of the instantaneous velocity and thermal field were visualized to analyze the structure of the vortices.

Abe at al. [14] reached Reynolds numbers of $Re_\tau \approx 640$ and 1020 for $Pr = 0.025$ and 0.71, in both cases. Seki et al. [15] made a simulation for $Re_\tau \approx 180$ and for $Pr = 0.71$, 1, 2 and 10. The values of $Pr = 0.025$ and $Pr = 10$ are, up to the knowledge of the authors, the lowest and highest values, respectively, used in a DNS of a thermal channel flow. To increase the Reynolds number, one of the alternatives would be to reduce the length and width of the computational box. This box, however, has to be large enough to accurately describe the flow. Lozano-Durán and Jiménez for isothermal channel flow [16], and Lluesma et al. for thermal ones [17], found out that a relatively small computational box of stream- and span-wise sizes of only $2\pi h \times \pi h$ can satisfactorily recover the one-point statistics of the flow. Using this box, Lluesma et al [17] ran a simulation for $Pr = 0.71$ and $Re_\tau = 2000$. Among other things, they found that for these two parameters the thermal flow shows the first stages of a thermal logarithmic layer for a thermal von Kármán constant of 0.44. This constant seems to be actually constant in the range of Reynolds numbers studied. In 2016, Pirozzoli et al. [18] ran different simulations for three different Prandtl numbers: 0.2, 0.71 and 1 using a simimilar boundary condition to [7]. Four different friction Reynolds numbers were used: 550, 1000, 2000 and, for the first time up to the knowledge of the authors, 4000. A comparison of Pirozzoli et al.'s data and the one obtained in this work is presented in section 3.5.

In this paper, moderated Reynolds numbers of values 500, 1000, and 2000 are simulated. The behaviour of the thermal flow for medium to low Prandtl numbers is studied. Table 1, summarizes the simulations made for this work. Already available simulations and the new ones are shown. Most of these simulations are new and, for the first time, Prandtl number below 0.01 have been simulated for turbulent channel flows. First order turbulent statistics and turbulent budgets have been obtained and will be discussed.

The structure of the paper is as follows. In the second section, the equations together with the numerical method and the different parameters of each simulation are described. In the third and fourth sections, the dynamics of the different flows are discussed. Finally, the fifth section contains the conclusions.

Pr | Re_τ	500	1000	2000
0.71	x [14]	x [14]	x [17]
0.5	∘	∘	∘
0.3	x [14]	x [18]	x [18]
0.1	x [14]	x [18]	x [18]
0.05	∘	∘	∘
0.02	x [14]	x [14]	∘
0.01	∘	∘	∘
0.007	∘	∘	∘

Table 1: Summary of cases studied. The x indicates a published simulation at close values of Re_τ and Pr. The ∘ denotes a new simulation.

2. Numerical procedure

2.1. Flow configuration and computational domain

In this work, a new set of DNS of a passive thermal flow in a Poiseuille turbulent channel has been conducted. The flow is considered incompressible, and heated by a uniform heat flux from both walls. The average walls temperature is independent with time and increases linearly along the streamwise direction. These conditions are known as Mixed Boundary Conditions (MBC).

A schematic representation of the computational box, with periodicity in the streamwise and spanwise directions, can be seen in Figure 1, where contours of the velocity are shown for the case $Re_\tau = 500$ and $Pr = 0.3$. The dimensions of the computational box are $2\pi h, 2h, \pi h$ in the streamwise, wall-normal and spanwise directions, respectively. Their correspondent spatial coordinates are represented by x, y and z, respectively. The velocities for each direction are U, V and W or, in index notation, U_i. The temperature is represented by T and the transformed temperate (see below) by Θ. Using the Reynolds decomposition any flow magnitude, denoted by uppercase letters, can be decomposed into its average part, which is denoted by an overbar, and its fluctuating part, which is denoted by lowercase letters, i. e. $U = \overline{U} + u$.

2.2. Governing equations and numerical schemes

The behaviour of thermal flows is characterized by the Navier Stokes equations, this is continuity and momentum equations,

Cases	Colour	Re	N_x	N_y	N_z
$\mathrm{Re}_\tau = 500$		10200	384	251	384
$\mathrm{Re}_\tau = 1000$		22300	768	383	768
$\mathrm{Re}_\tau = 2000$		48500	1536	633	1536

Prandtl	0.71	0.5	0.03	0.01	0.05	0.02	0.01	0.007
Symbol	△	⬠	▷	◁	◯	□	◇	▽

Table 2: Parameters of the simulation. Three different Reynolds numbers for eight different Prandtl numbers have been simulated. The third column shows the bulk Reynolds numbers. N_x, N_y and N_z are the number of collocation points in each of the three directions of the computational box. Line colours (second column) and symbols (second table) are used to identify the cases through all the figures of this article.

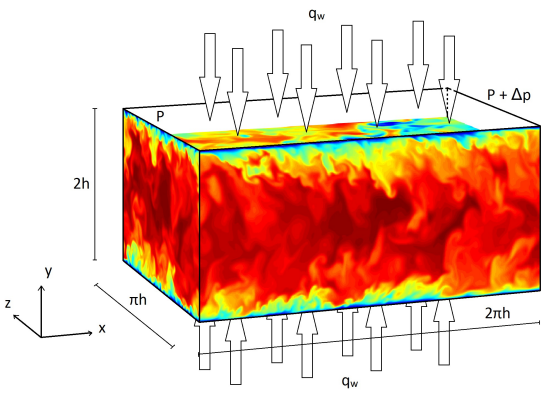

Figure 1: Schematic representation of the computational box. The flow is driven by a constant pressure gradient and moves from the left to the right. Both walls are considered adiabatic, and the thermal heat flux, q_w, is constant. The thermal flow is shown for $Re_\tau = 500$ and $Pr = 0.3$.

$$\partial_t U_i^+ + U_j^+ \partial_j U_i^+ = -\partial_i P^+ + \frac{1}{Re_\tau}\partial_{jj} U_i^+, \quad (1)$$

$$\partial_j U_j^+ = 0, \quad (2)$$

and the energy equation,

$$\partial_t \Theta^+ + U_j^+ \partial_j \Theta^+ = \frac{1}{Re_\tau Pr}\partial_{jj}\Theta^+ + U_1^+ / \langle U^+ \rangle_{xyz}. \quad (3)$$

For this last equation, the transformed temperature, defined as $\Theta = T - T_w$, has been used to satisfy the MBC. In the streamwise direction, the hypothesis is that temperature increases linearly. Subtracting T_w to T makes Θ periodic, as T_w carries the non-periodic part of the thermal flow. Among other things, this allows the use of highly efficient Fourier methods in the streamwise direction. In order to solve equations (1), (2) and (3), the same method that was used in [17] has been employed. This method is based on the velocity-vorticity method developed in [7]. The Navier Stokes equations are transformed into equations for the wall-normal vorticity, Ω_y, and the Laplacian of the wall-normal velocity, Φ. Then, the rest of variables can be recovered from these two fields using continuity and vorticity equations. For the spatial discretization, dealiased Fourier expansions in the x and z direction are implemented. The y direction is discretized through a seven-point compact finite differences scheme with fourth-order consistency and extended spectral-like resolution [19]. The temporal discretization is a third-order semi-implicit Runge-Kutta scheme [20].

2.3. Simulation parameters

Tables 2 and 3 show the mesh information for the different simulations performed. The number of points in the y direction are chosen in such a way that the spacing obtained is proportional to the local isotropic Kolmogorov scale $\eta = \left(\nu^3/\epsilon\right)^{1/4}$. The increment in y is set to be $\Delta y = 1.5\eta$. Therefore, the wall normal resolution in the wall in physical space is $\Delta y^+ = 0.72$, 0.44 and 0.32, for $Re_\tau = 500$, 1000 and 2000, respectively. In the center of the channel, the resolution is $\Delta y^+ = 5.3$, 7.4 and 8.8, for $Re_\tau = 500$, 1000 and 2000, respectively. On the other hand, the streamwise and spanwise resolution in physical space is $\Delta x^+ \sim 8.18$ and $\Delta z^+ \sim 4.09$. These values are similar to many other trusted simulations [12, 14, 17, 21, 22]. The code used for this simulation is a variation of LISO code [21, 22, 23, 24] for thermal flows that was validated in [17].

The procedure to run the simulation is the same as in other works [17, 21, 22, 23, 24]. For every case one Reynolds and one Prandtl number are chosen. An initial file is used to initialize the simulation. This initial file has been taken form a similar case previously simulated. When the variables of the simulation have reached a statistically steady state, statistics of the flow are collected. As a first rule of thumb, the simulations were run for 20 wash-outs, where a wash-out is the time needed for an

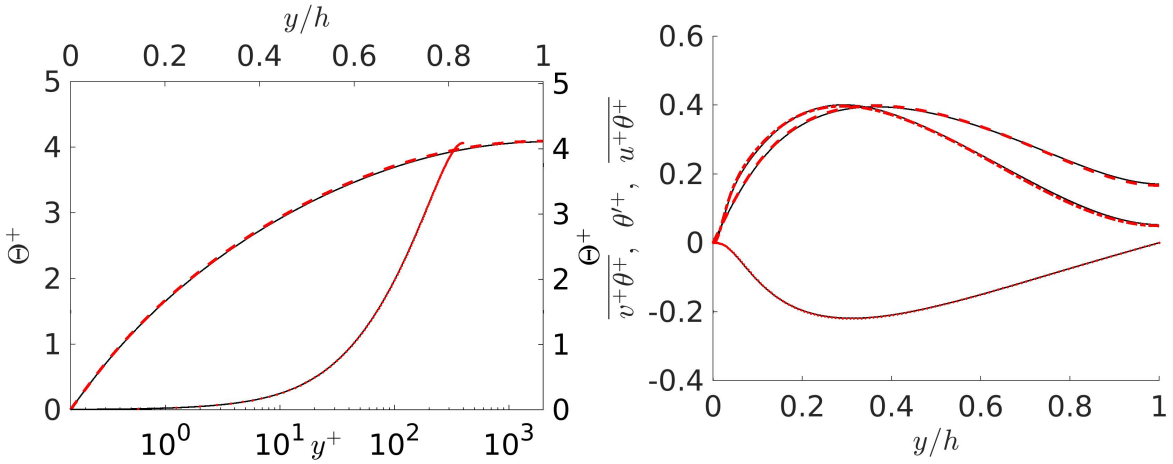

Figure 2: Colour online. (a) Mean temperature profile in inner (bottom, dashed line) and outer (top, pointed line) scales for $Re_\tau = 400$ and $Pr = 0.025$. (b) Temperature RMS (dashed) and streamwise (dash-pointed) and wall-normal (pointed) heat fluxes. Black solid lines from Kawamura's database [14].

Δ	Wall	Center
x^+	8.18	
z^+	4.09	
y^+ ($Re_\tau = 500$)	0.72	5.3
y^+ ($Re_\tau = 1000$)	0.44	7.4
y^+ ($Re_\tau = 2000$)	0.32	8.8

Table 3: Physical resolution in x, y and z directions, at the wall and in the center line.

eddy to cross the channel. However, before reaching the statistically steady state, there exists a transition phase in which the variables have to adapt to the new values of Re_τ and Pr. This convergence, especially for the temperature variable, is very time consuming and it can be as long as the time needed to gather all the statistics. In order to overcome this problem, the expected mean temperature of the initial field has been extrapolated from previous simulations, reducing the convergence time to a negligible fraction of the total simulation time.

In order to validate the code for lower Prandtl numbers, a simulation for $Re_\tau = 400$ and $Pr = 0.025$ has been performed. This Prandtl number is, up to the knowledge of the authors, the lowest Prandtl number simulated in turbulent channel flows and was done first by Abe et al [14]. The results of the simulation have been compared with the data provided in Kawamura's database [14]. This comparison is shown in Figure 2. Figure 2a shows a perfect agreement for the mean temperature in both inner and outer scales. Also, in figure 2b all curves collapse almost perfectly for the temperature variance and both heat fluxes. The very small differences can be due to small statistical uncertainties during the simulation, a slightly different Reynolds number or a different numerical scheme.

In order to further validate the database, an optimum averaging time of the simulation for statistical convergence could have been used as in [25]. Instead, the total heat flux has been calculated and compared with the molecular and turbulent heat fluxes. These equations come from integration of equation (3),

$$q^+_{total} = \overbrace{\frac{1}{Pr}\frac{d\overline{\Theta}^+}{dy^+}}^{\text{Molecular}} \overbrace{-\overline{v^+\theta^+}}^{\text{Turbulent}} = \overbrace{1 - \frac{1}{Re_\tau}\int_0^{y^+} \frac{U_1^+}{\langle U^+\rangle_{xyz}}\, dy}^{\text{Total}}. \tag{4}$$

In Figure 3, all three heat fluxes are represented for all Prandtl numbers at $Re_\tau = 1000$ and 2000. Molecular and turbulent heat fluxes are compared with the total one and the difference is obtained. It has been considered that enough statistics were obtained when this difference was below 10^{-3}. As a first result, turbulent heat flux decreases for lower Prandtl numbers. This entails a thermal flow that is less turbulent. The magenta line is formed by the cross points between the molecular and turbulent heat fluxes. For a certain value of Prandtl, turbulent heat flux is lower than molecular heat flux in all the channel. This value of the Prandtl number increases with the Reynolds number, since a higher Re entails a more turbulent flow.

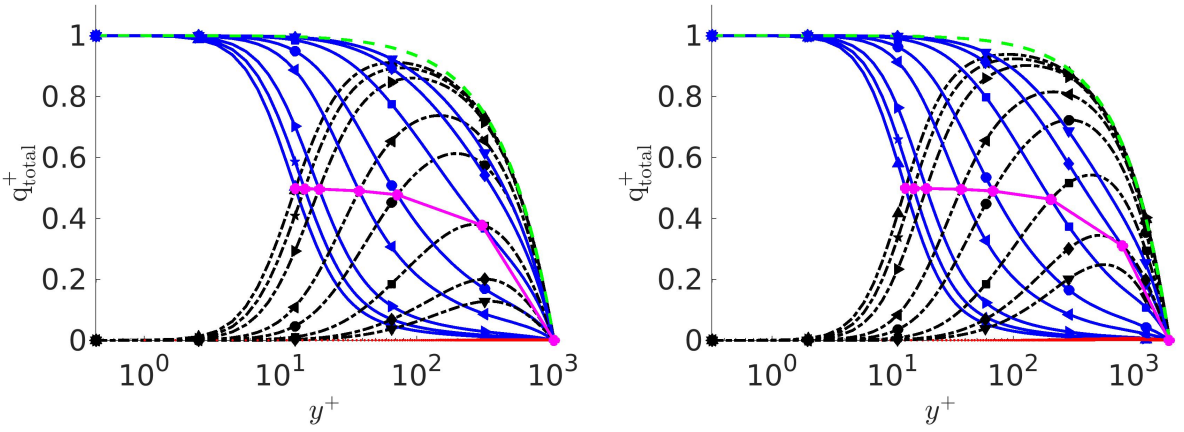

(a) (b)

Figure 3: Colour online. Heat fluxes for (a) $Re_\tau = 1000$ and (b) $Re_\tau = 2000$. Molecular (blue solid), turbulent (black, dash-dot) and total (green, dashed) heat fluxes. Red pointed line represents the difference between the LHS and RHS of equation 4. Magenta solid line is formed by the cross points between molecular and turbulent heat fluxes. Simbols as in Table 2.

3. Results

3.1. Instantaneous visualizations

The instantaneous visualizations of the velocity and thermal fields for different simulations for $Re_\tau = 2000$ are shown in Figure 4. The objective is to compare the turbulent scales and see how a decrease in the Prandtl number affects to these scales. In figure 4a, the velocity field for $Pr = 0.71$ is shown. These turbulent scales are comparable to the ones presented in the thermal field for the same Prandtl number, figure 4b. This result was expected since $Pr \sim 1$ and, therefore, $Pe_\tau \sim Re_\tau$.

As equations (1-3) are solved for each case, the velocity field for $Pr = 0.05$ and $Pr = 0.007$ is similar to the one presented in figure 4a. However, the instantaneous temperature fields shown in figures 4c and 4d, respectively, are different. For low Prandtl number the thermal flow becomes less turbulent and, for the smallest case studied, the thermal flow is almost laminar. This confirms once again that reducing the Prandtl number, the thermal field is less turbulent, reducing the turbulent heat flux and the heat transfered by convection.

3.2. Mean temperature profiles

Mean temperature profiles are shown in figure 5a. Keeping Pr constant, all Θ^+ collapse in the near-wall and logarithmic region. In the central zone, when Re_τ increases, temperature profiles go deeper and, for the same Pr, the slope of the line slightly decreases.

An important parameter that can be derived from the mean temperature profile is the thermal von Kármán constant, κ_t. For sufficiently high Pr numbers, the mean temperature profile can be described in the logarithmic region with the following relation

$$\Theta^+ = \frac{1}{\kappa_t} \ln(y^+) + B. \tag{5}$$

The classic limits for this logarithmic region for the streamwise velocity are $y^+ \approx 70$ and $y/h = 0.2$, according to Jiménez [26]. The same limits have been used for the thermal flow. Even if a logartimic layer is not really present until a higher Reynolds is reached [27, 28, 29], an indicator of this region is the first minimum of the diagnosis function. This first minimum, and thus a logarithmic layer, appears for Prandtl numbers greater than approximately 0.3. It is worthy to stress that all the calculations shown below are a first approximation to the actual value of κ_t. A truly logarithmic layer is not expected untill at least $Re_\tau \approx 5000$.

The values of κ_t and B are collected in Table 4. Notice that the value of κ_t increases slightly with an increase of the Re_τ number, for the smaller Reynolds number. This is caused by a slight reduction of the slope of $\overline{U}$ in the logarithmic region for the same Pr when Re_τ is increased. However, for $Re_\tau \geq 1000$, κ_t seems to be, indeed, constant, with an approximate value of 0.44. This result agrees with the one obtained by Abe et al [14]. The constant B changes for each Prandtl number. For $Pr = 0.71$, a value of $B \approx 3$ is obtained, which also agrees with the one obtained by Abe et al [14]. When the Prandtl number is reduced to 0.5 and 0.3, the values of B are reduced to approximately 0.6 and -1.9, respec-

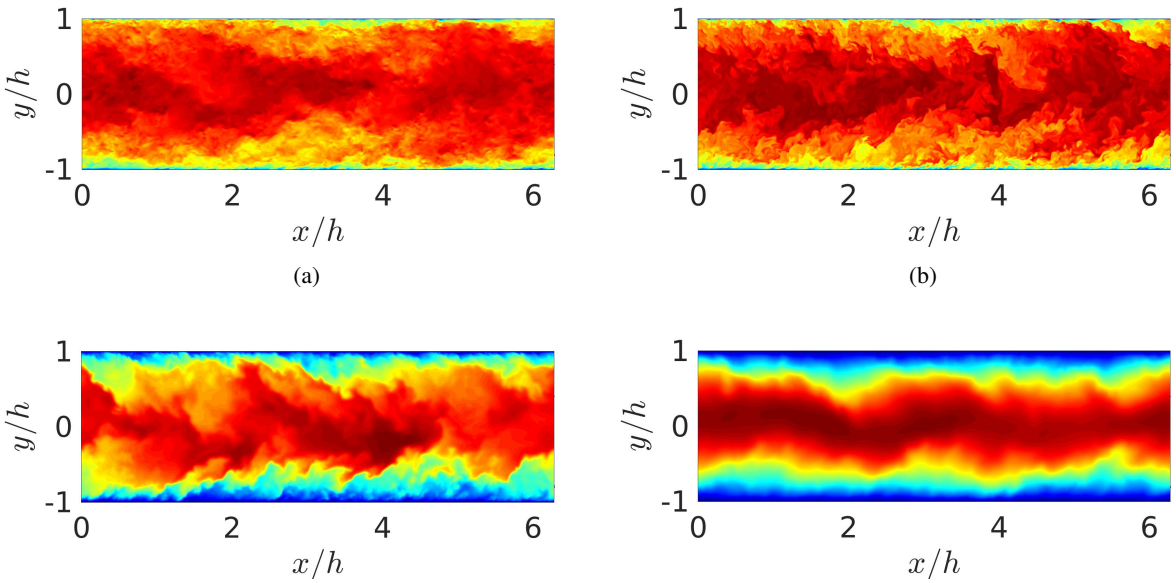

Figure 4: Instantaneous visualizations for $Re_\tau = 2000$ and (a) velocity field for $Pr = 0.71$, (b) thermal field for $Pr = 0.71$, (c) thermal field for $Pr = 0.05$ and (d) thermal field for $Pr = 0.007$.

tively.

	κ_t	Re_τ 500	1000	2000
	0.71	0.417846	0.436265	0.439748
Pr	**0.5**	0.419616	0.434211	0.435943
	0.3	0.426754	0.438126	0.436668

	B	Re_τ **500**	**1000**	**2000**
	0.71	2.888235	3.107018	3.052149
Pr	**0.5**	0.548110	0.703806	0.641138
	0.3	-1.988293	-1.870591	-2.000945

Table 4: Thermal von Kármán constant and B values.

To further explore this logarithmic region, the thermal diagnosis function, defined as

$$\Xi_T = y^+ \partial_{y^+} \overline{\Theta^+}, \tag{6}$$

is used. In figure 5b, Ξ_T is plotted for all cases. It can be seen how for the three greater Pr numbers, there exist two maximum values. The y^+ location of the first maximum does not depend on Re_τ. However, its value decreases slightly for an increase in the Reynolds number. When the Prandtl number is decreased below 0.3, this first maximum disappears and, therefore, the logarithmic region. On the other hand, the y^+ coordinate of the second maximum is independent of Pr. In outer coordinates (not shown), the position of the second maximum is independent of both Re_τ and Pr and it is located at $y/h = 0.5$. It has been observed that the value of Ξ_T at this second maximum is constant for $Pe_\tau > 30$. When this Péclet number is reduced below 30, the value of second maximum is then reduced. Therefore, the behaviour of the second maximum cannot be characterized only by Pr.

3.3. Nusselt number

Coming back to figure 5a, black lines represent the thermal law of the wall, $\Theta^+ = Pr \cdot y^+$. In the conduction region of the flow, Θ^+ behaves approximately according to this law. It can be seen that a decrease in the Pr number entails a bigger conductive region. Therefore, an increase in the heat transfer by conduction is expected.

The Nusselt number is calculated according to the following definition [12]

$$Nu = \frac{L\mathfrak{h}}{\kappa} = \frac{2Re_\tau Pr}{\langle\Theta^+\rangle_{xyz}} = \frac{2Pe_\tau}{\langle\Theta^+\rangle_{xyz}}, \tag{7}$$

where L is a characteristic length, in this case it is the channel height of the computational box, $2h$; $\mathfrak{h}$ is the convective heat transfer coefficient; and κ is the thermal

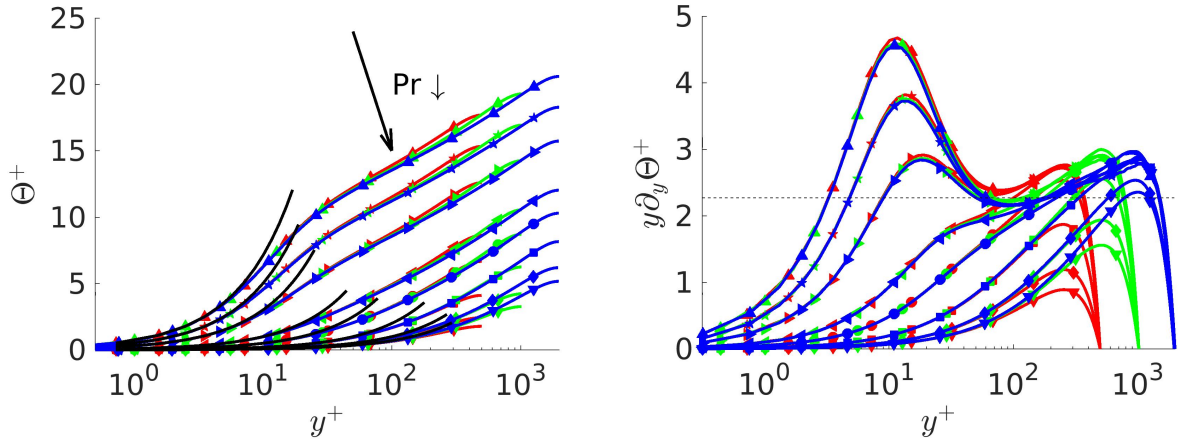

(a) (b)

Figure 5: Colour online. (a) Mean temperature profile. Black lines correspond to the thermal law of the wall. (b) Thermal diagnosis function. The dashed horizontal line corresponds to a thermal von Kármán constant of 0.44. Colours and lines as in Table 2.

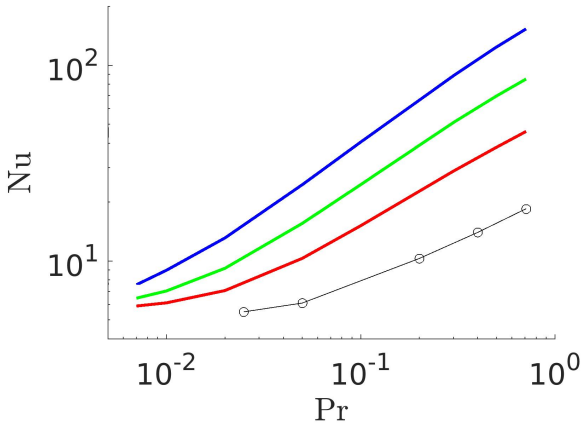

Figure 6: Colour online. Nusselt number. Thin black line from Kawamura et al [12] for $Re_\tau = 180$. Colours and lines as in Table 2.

conductivity. According to this definition, the minimum Nusselt number that can be obtained for the present configuration is 4. In such a case, temperature will behave following the thermal law of the wall in the entire channel. In Figure 6, obtained Nusselt number are plotted as a function of the Prandtl number. Up to the knowledge of the authors, it is the first time that these results are provided for Prandtl numbers of 0.01 and 0.007 and $Re_\tau > 500$. Nusselt number was calculated by Kawamura et al [12] for $Re_\tau = 180$ and Prandtl numbers from 0.025 to 5. They found that in the range of Prandtl between 0.2 and 1.5, Nu had a linear logarithmic increment. This agrees with the results obtained in this paper for larger Re numbers. In addition, it is seen that the range of Prandtl numbers where Nu has a linear logarithmic increment is larger when Re is increased (at least the lowest limit is reduced). As it was expected, the Nusselt number decreases with Re_τ or Pr numbers. This entails in a decrement of the heat transfered by convection.

3.4. Temperature and heat fluxes intensities

The root mean square of the temperature variance, θ'^+, and the heat fluxes in the streamwise, $\overline{u^+\theta^+}$, and wall-normal, $\overline{v^+\theta^+}$, directions are represented in Figure 7. All $Re_\tau = 2000$ cases are plotted as a function of y/h in figures 7a and 7c. Meanwhile, in figures 7b and 7d, the same functions are plotted for all three Reynolds numbers of study and for three different Prandtl numbers: 0.71, 0.3 and 0.02. The tendency of the results of these turbulent intensities agrees perfectly with the results obtained by Abe et al [14] and Kawamura et al [12].

First at all, in figure 7a, for Prandtl numbers greater than approximately 0.3, θ'^+ tends to collapse in the outer region, approximately for $y/h > 0.3$. However, when Re_τ is reduced (figure 7b), the value of Pr at which θ'^+ collapses increases. It is observed again, that the use of the Péclet number gives a good approximation to determine which cases collapse in the central region of the channel. For $Pe_\tau > 325$, θ'^+ tends to collapse for $y/h > 0.3$. The maximum value of θ'^+ increases when Re_τ increases. The location of this maximum depends on the Prandtl number. On the one hand, when Pr is greater than approximately 0.3, the y^+ coordinate of the

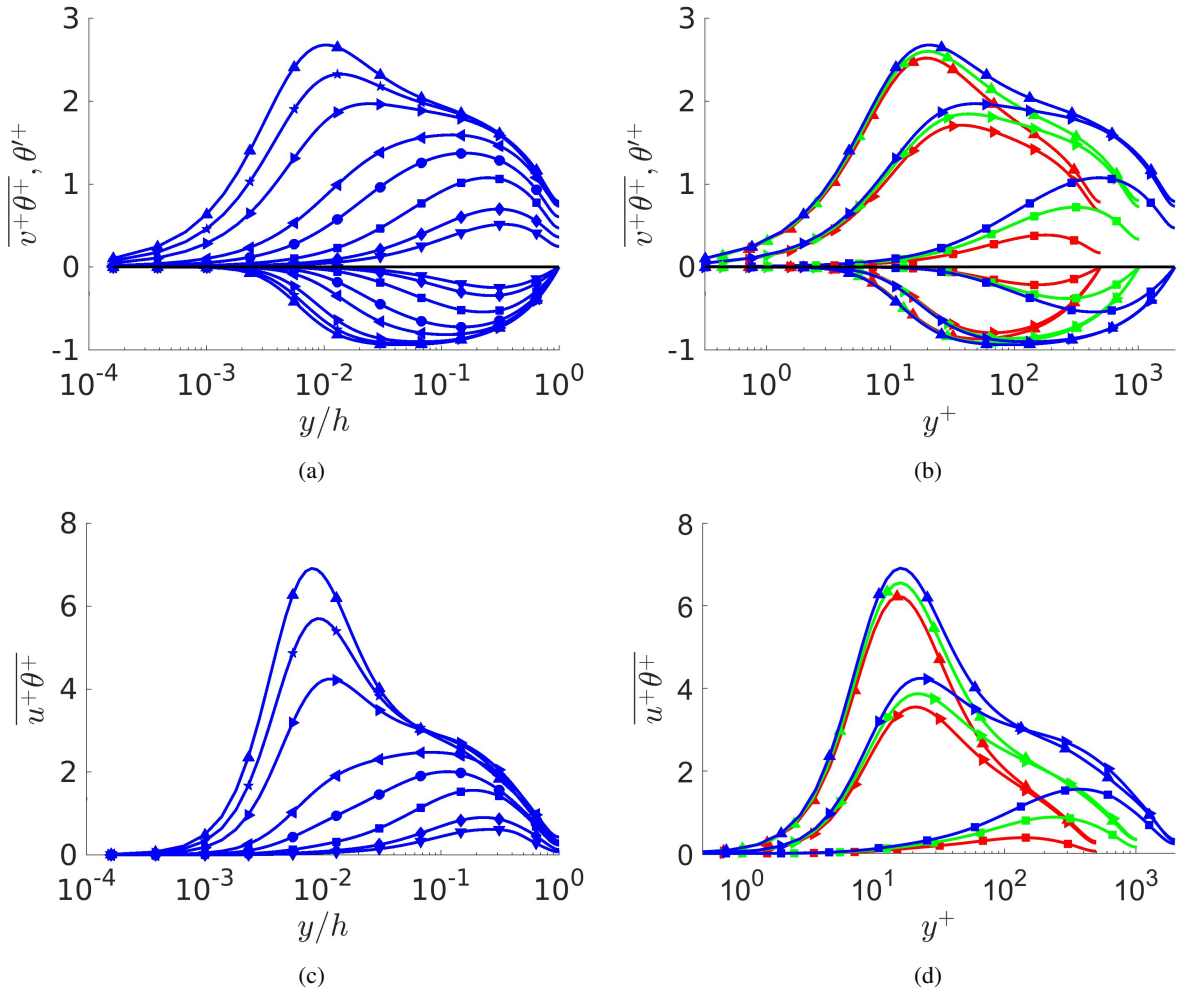

Figure 7: Colour online. Root mean square of the temperature variance and wall-normal heat flux for (a) $Re_\tau = 2000$ as a function of y/h and (b) $Pr = 0.71$, 0.3 and 0.02 as a function of y^+. Streamwise heat flux for (c) $Re_\tau = 2000$ as a function of y/h and (d) $Pr = 0.71$, 0.3 and 0.02 as a function of y^+. Colours and lines as in Table 2.

maximum is independent of the Re_τ number. In such cases, it is located in the buffer layer or logarithmic region. On the other hand, for Pr lower than 0.3 the morphology of θ'^+ changes. Now, its maximum location moves to the outer region. For these cases, the coordinate y^+ of the maximum depends on both Reynolds and Prandtl numbers.

In the same way as θ'^+, all the profiles for $\overline{v^+\theta^+}$ (figure 7a) collapse in the outer region, for $y/h > 0.1$ and Péclet numbers greater than approximately 225. The minima location of $\overline{v^+\theta^+}$ is always in the outer region. This location depends on both the Reynolds and Prandtl numbers.

Finally, $\overline{u^+\theta^+}$ is shown in figures 7b and 7d. The behaviour of this function is the same as the previous turbulent intensities. Values collapse from $y/h = 0.07$ up to the center of the channel when $Pe_\tau > 325$. Regarding to the location of the function maxima, the analysis is the same as for θ'^+, and the threshold is again $Pr \approx 0.3$. For Prandtl numbers above this threshold, these maxima are located in the buffer layer or logarithmic region. Their positions are independent of the Re_τ number. For the lower Prandtl numbers, the y^+ coordinate of the maxima depends on both Re_τ and Pr. These similitudes between θ'^+ and $\overline{u^+\theta^+}$ come from the high correlation that exist between them. However, as the Péclet number is reduced, this correlation is also reduced, and the differences between the different profiles are increased.

As a general rule, one can conclude that the location

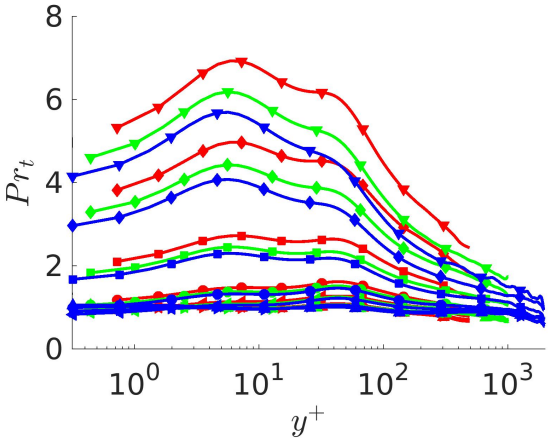

Figure 8: Colour online. Turbulent Prandtl number. Colours and lines as in Table 2.

of the maxima does not depend on the Reynolds number when the maximum is located in the buffer layer or in the logarithmic region. However, for lower Prandtl numbers, the maxima location moves to the outer region. Here, it does depend on the Reynolds number.

In every case, the values of the root mean square of the temperature variance and both heat fluxes decrease when Pr decreases. This means that, for lower Prandtl numbers, turbulent intensities decreases, in other words, the thermal flow is less turbulent. This confirms the result obtained during the validation of the simulation, when molecular and turbulent heat fluxes were obtained.

3.5. Boundary conditions influence

As it was explanied in the introduction the MBC was used in the simulations of the present work. The results obtained for the cases of $Pr = 0.71$ and $Re_\tau = 1000$ and 2000 are now compared with the ones calculated by Pirozzoli et al. [18]. For that work, a spatially uniform forcing was adopted as the boundary condition of the thermal equation, in the same way as in [7]. Therefore, one cannot expect to obtain the same results, but the tendencies of the temperature and its intensities would not differ abruptly.

In Figure 9, the mean temperature, the root mean square of the temperature variance, and the streamwise and wall-normal heat fluxes are represented, in figures 9a, 9b, 9c and 9d, respectively. Indeed, all magnitudes increase when the MBC is used, specially in the central region of the channel. Values for $Pr = 0.71$ and $Re_\tau = 4000$ obtained in [18] are also represented with the dashed black line to visualize the tendency of the variables when increasing the Reynolds number.

Nu	Present work	Pirozzoli et al.
$Re_\tau = 1000$	85.0416	86.0682
$Re_\tau = 2000$	153.378	159.854

Table 5: Comparison of the Nusselt number for $Pr = 0.71$ and $Re_\tau = 1000$ and 2000 with the ones obtained by Pirozzoli et al. [18].

With respect to the Nusselt number, Table 5 shows a comparison between the Nusselt numbers obtained for $Pr = 0.71$ and $Re_\tau = 1000$ and 2000 in the present work and the ones obtained in [18]. A decrease in the value of Nu is obtained when the MBC is used. This was expected, since the temperature profiles were slightly greater. Nevertheless, the results are reasonably similar.

3.6. Turbulent Prandtl number

The turbulent Prandtl number is defined as the ratio between the momentum eddy diffusivity, ν_t, to the thermal eddy diffusivity, κ_t,

$$Pr_t = \frac{\nu_t}{\kappa_t} = \frac{\overline{uv}}{\overline{v\theta}} \frac{d\overline{\Theta}/dy}{d\overline{U}/dy}. \tag{8}$$

Pr_t is shown, as a function of y^+, in Figure 8. These results reaffirm the well-known law that states that Pr_t is approximately constant and equal to 1 for medium to high molecular Prandtl numbers but it increases for low Prandtl numbers (Kawamura et al [12]). It can be seen how for $Pr <= 0.05$ the values of Pr_t are higher, not only in the wall vicinity but along all the channel. In addition, an increase in the Reynolds number entails a slightly decrease in the turbulent Prandtl number. Therefore, new scaling laws for low Prandtl numbers are needed.

4. Turbulent budgets

Budgets of the turbulent heat fluxes, $\overline{u_i\theta}$, the temperature variance, $k_\theta = 1/2\,\theta^2$, and the dissipation rate of the temperature variance, $\varepsilon_\theta = \frac{1}{Pr}\overline{\partial_i\theta\partial_i\theta}$ have been calculated. The equations that define them can be obtained from [30].

The budget equation for the turbulent heat fluxes, $\overline{u_i\theta}$, is given by

$$\frac{D\overline{u_i\theta}}{Dt} = P_i + T_i + V_i + \Pi_i^s + \Pi_i^d + \varepsilon_i, \tag{9}$$

where D/Dt is the mean substantial derivative.

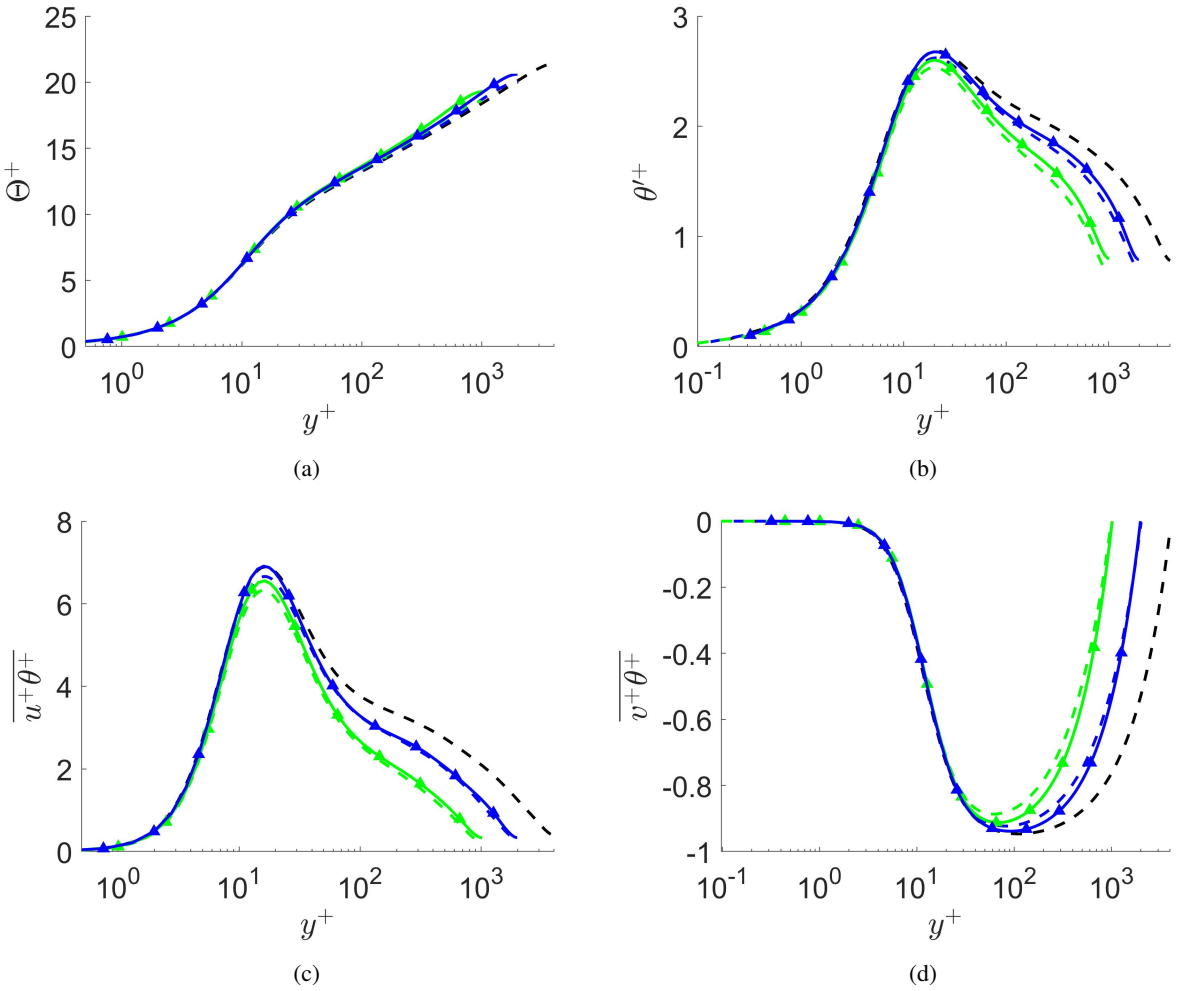

Figure 9: Colour online. Comparison of the temperature and its intensities for $Pr = 0.71$ and $Re_\tau = 1000$ and 2000 with the ones obtained by Pirozzoli et al. [18]. (a) Mean temperature profile, (b) root mean square of the temperature variance, (c) streamwise heat flux and (d) wall-normal heat flux. Dashed lines reperents data from Pirozzoli et al. Black dashed lines represent values for $Pr = 0.71$ and $Re_\tau = 4000$ from Pirozzoli et al. Colours and lines as in Table 2.

The different terms on the right hand side are referred to as production, turbulent diffusion, viscous or molecular diffusion, pressure-temperature gradient correlation, pressure diffusion and dissipation. They are respectively defined according to

$$P_i = -\overline{u_i v}\partial_y\overline{\Theta} - \overline{v\theta}\partial_y\overline{U_i}, \tag{10a}$$

$$T_i = -\partial_{x_k}\overline{u_i u_k \theta}, \tag{10b}$$

$$V_i = \nu\partial_{x_k}\left(\overline{\theta\partial_{x_k}u_i} + \frac{1}{Pr}\overline{u_i\partial_{x_k}\theta}\right), \tag{10c}$$

$$\Pi_i^s = \overline{p\partial_{x_i}\theta}, \tag{10d}$$

$$\Pi_i^d = -\partial_{x_k}\left(\delta_{ki}\overline{p\theta}\right), \tag{10e}$$

$$\varepsilon_i = -\nu\left(1 + \frac{1}{Pr}\right)\overline{\partial_{x_k}u_i\partial_{x_k}\theta}. \tag{10f}$$

In the previous definitions, δ_{ij} is Kronecker's delta

and repeated index imply summation over $k = 1, 2, 3$. The transport equation of k_θ involves production, turbulent diffusion, viscous diffusion and dissipation terms,

$$\frac{D\overline{k_\theta}}{Dt} = P + T + V + \varepsilon_\theta. \tag{11}$$

These terms are defined as

$$P = -\overline{v\theta}\partial_y\overline{\Theta}, \tag{12a}$$

$$T = -\frac{1}{2}\partial_y\overline{\theta^2 v}, \tag{12b}$$

$$V = \frac{1}{2Pr}\partial^2_{yy}\overline{\theta^2}, \tag{12c}$$

$$\varepsilon_\theta = -\frac{1}{Pr,}\overline{\partial_i\theta\partial_i\theta}. \tag{12d}$$

Finally, the transport equation for ε_θ is given by

$$\frac{D\overline{\varepsilon_\theta}}{Dt} = P_m + P_{mg} + P_g + P_t + T_t + V_{\varepsilon_\theta} + \varepsilon_{\theta 1}. \tag{13}$$

In this case, the terms are named mixed production, mean gradient production, gradient production, turbulent production, turbulent transport, molecular diffusion and dissipation.

$$P_m = -\frac{2}{Pr}\overline{\partial_i v\partial_i\theta}\partial_y\overline{\Theta}, \tag{14a}$$

$$P_{mg} = -\frac{2}{Pr}\overline{\partial_x\theta\partial_y\theta}\partial_y\overline{U}, \tag{14b}$$

$$P_g = -\frac{2}{Pr}\overline{v\partial_y\theta}\partial^2_{yy}\overline{\Theta}, \tag{14c}$$

$$P_t = -\frac{2}{Pr}\overline{\partial_i\theta\partial_j\theta\partial_j u_i}, \tag{14d}$$

$$T_t = -\frac{1}{Pr}\partial_y\overline{v\partial_i\theta\partial_i\theta}, \tag{14e}$$

$$V_{\varepsilon_\theta} = \frac{1}{Pr^2}\partial^2_{yy}\varepsilon_0, \tag{14f}$$

$$\varepsilon_{\theta 1} = -\frac{2}{Pr^2}\overline{\partial^2_{kj}\theta\partial^2_{kj}\theta}. \tag{14g}$$

For the thermal heat fluxes, Figures 10 and 11, the data has been adimensionalized by $\nu/u_\tau^3\theta_\tau$. For the temperature variance, Figure 12, the term $\nu/u_\tau^2\theta_\tau^2$ has been used. Finally, the dissipation rate of the temperature variance, Figure 13, employs $\nu^3/u_\tau^4\theta_\tau^2$. In the latter figure, the four production terms have been sum up to facilitate the discussion. In previous works, [17] or [31], turbulent budgets were obtained for $Pr = 0.71$. The idea of this section is to check whether these scaling laws work or not for low values of the Prandtl number. As an anticipated result, for low Prandtl numbers, any of the scaling laws work.

Budgets for $\overline{u^+\theta^+}$ are shown in Figure 10. Cases for $Re_\tau = 2000$ and medium Prandtl numbers (0.71, 0.3 and 0.1) are plotted in figure 10a. For the same Reynolds, the lowest Prandtl numbers (0.01 and 0.007) are selected for figure 10b. On the other two subfigures, the analysis is done for a variation of Re_τ. Budget terms for one of the medium Prandtl numbers, 0.1, are plotted for all three Reynolds numbers in figure 10c. Meanwhile, the lowest Prandtl, 0.007, is used, again for all three Reynolds numbers, in figure 10d. For both, medium and low Prandtl numbers, dissipation is compensated by viscous diffusion near the wall. From the end of the buffer layer up to the center of the channel, the production term increases and becomes more important than the viscous diffusion. In this part of the channel, for medium Prandtl numbers (figures 10a and 10c), dissipation and pressure-temperature gradient correlation terms are compensated by production. However, for low values of Pr (figures 10b and 10d), production compensates dissipation, and the rest of terms are negligible. Regarding the scaling law, it can be seen that it presents several errors when Pr varies (figures 10a and 10b). Not only the magnitudes of all the budget terms change along the entire channel, but also the location of the maximum changes depending on the Prandtl number. When Pr is kept constant and with a medium value (figure 10c) all terms seems to scale well in the logarithmic layer and in the center of the channel (difference are due to the difference in Re_τ). However, in the wall vicinity, viscous diffusion and dissipation present noticeable differences from one case to another. When Pr is reduced (figure 10d), these differences are even larger.

Budgets for $\overline{v\theta}$ are shown in Figure 11. The arrangement of the subfigures is the same as for the streamwise heat flux. It can be seen how for medium Prandtl numbers (figures 11a and 11c) the more important budget terms are pressure-temperature gradient correlation, pressure diffusion and production. However, when Pr is reduced (figures 11b and 11d), dissipation becomes more important than both pressure terms. For the lowest Prandtl numbers, these pressure terms become negligible and dissipation is compensated by the production term. Dissipation becomes more important for lower Prandtl numbers since it occurs in eddies of a larger scale, as it has been seen before in Figure 4. Regarding the scaling law, the same problems as for $\overline{u\theta}$ appear. For a constant Re_τ (figures 11a and 11b), the magnitude of the budget terms and the location of their maxima do not scale properly. When Pr is kept constant with value 0.1 (figure 11c) all terms seems to scale well except for

the pressure terms in the near wall region. For the lowest Prandtl number (figure 11d) scaling failures are seen in the center of the channel for the production and dissipation terms.

Budget terms for $\overline{k_\theta}$ are shown in Figure 12. Again, the sub-figures information is presented in the same order as in the previous ones. For all cases, dissipation is compensated by molecular diffusion in the wall vicinity and by production in the center of the channel. The y^+ coordinate where the production term becomes more important than molecular diffusion increases with a decrease of the Prandtl number. Turbulent diffusion appears to be more noticeable at the end of the buffer layer for medium Prandtl numbers. The scaling law used for these budget terms presents the same problems as before when a variation in the Prandtl number is introduced (figures 12a and 12b). In addition, the problem for the dissipation term is even more complex. In the buffer layer, not only the magnitude of this term changes, but also its morphology. For a variation of Reynolds and $Pr = 0.1$ (figure 12c), the same scaling problem for dissipation arises again. Molecular and turbulent diffusions also present scaling problems in the buffer layer. For the lowest Prandtl number (figure 12d) a better scaling law is needed.

Finally budget terms for $\overline{\varepsilon_\theta}$ are shown in Figure 13. The cases shown in each sub-figure are the same as in the previous analysis. Dissipation is mostly compensated by production, except in the wall vicinity, where viscous diffusion is not negligible. For lower Prandtl numbers, the effect of viscous diffusion close to the wall is more remarkable. The scaling law used for $\overline{\varepsilon_\theta}$ present the same problems for variations of Prandtl numbers (figures 13a and 13b). When the Reynolds number is changed and $Pr = 0.1$ (figure 13c) scaling errors appear in the logarithmic region for production and dissipation terms. Also, in the buffer layer, the viscous diffusion term does not scales properly. For $Pr = 0.007$ (figure 13d), the differences in the production and dissipation terms are larger.

In general, it is seen that scaling laws fail for lower Prandtl numbers, especially in the near wall region. The more conflictive terms are dissipation and viscous diffusion. Also, remark the scaling errors in the pressure terms for $\overline{v\theta}$ and the production term for $\overline{\varepsilon_\theta}$. It has been seen through all the article that the behaviour of the thermal field changes for low Prandtl numbers. Therefore, one could have expected these scaling differences. This suggest that the modeling of some of the budget terms depends on both Re_τ and Pr, which makes their modeling a very complex problem.

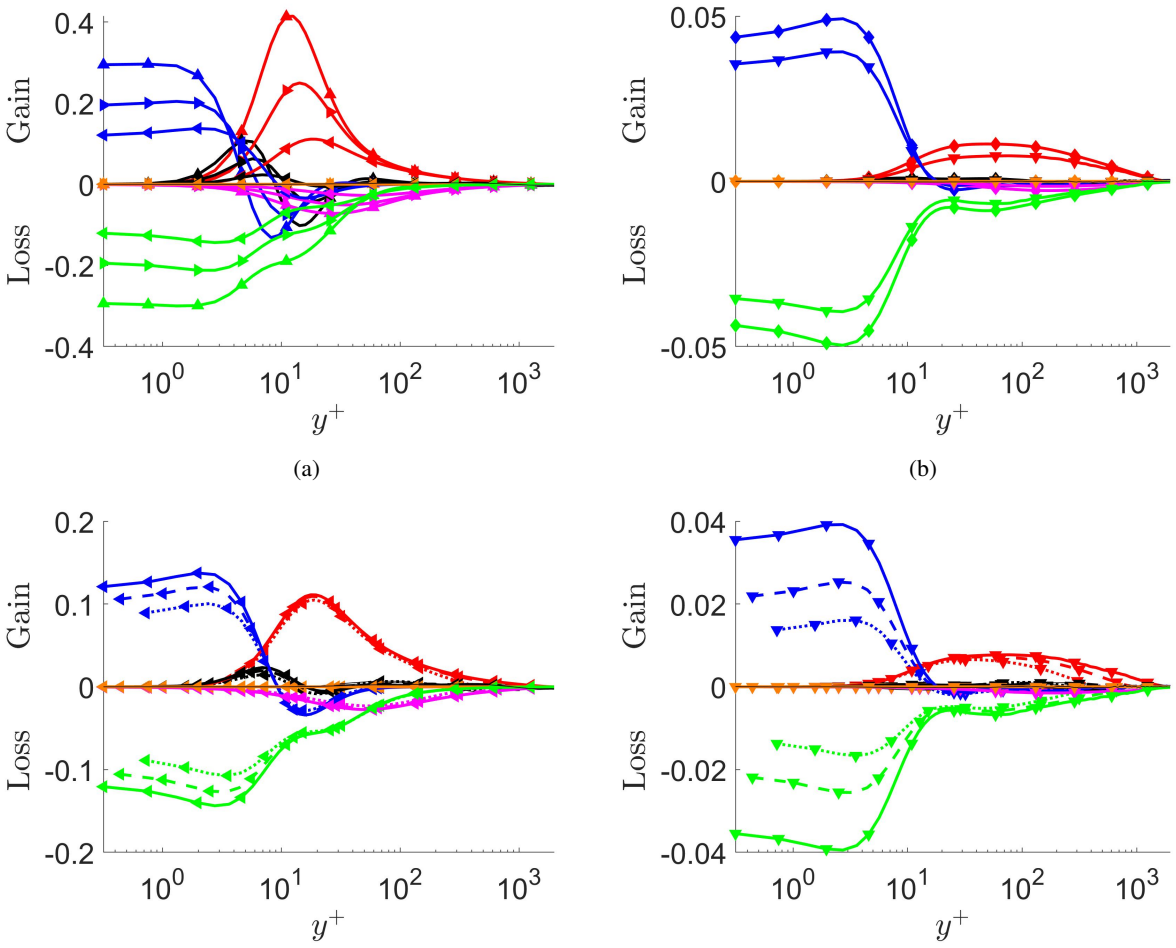

Figure 10: Colour online. Budgets of the streamwise heat flux, $\overline{u\theta}$, for $Re_\tau = 2000$ and (a) medium Prandtl numbers: $Pr = 0.71$, 0.3 and 0.1; (b) low Prandtl numbers: $Pr = 0.01$ and 0.007. $Re_\tau = 2000$, 1000 and 500 for (c) $Pr = 0.1$ and (d) $Pr = 0.007$. Colours here denote budget terms: production (red), turbulent diffusion (black), viscous diffusion (blue), dissipation (green), pressure-temperature-gradient correlation (magenta) and pressure diffusion (orange). Line style determines the Re_τ number: $Re_\tau = 2000$ (solid line), $Re_\tau = 1000$ (dashed line) and $Re_\tau = 500$ (pointed line). Symbols as in Table 2.

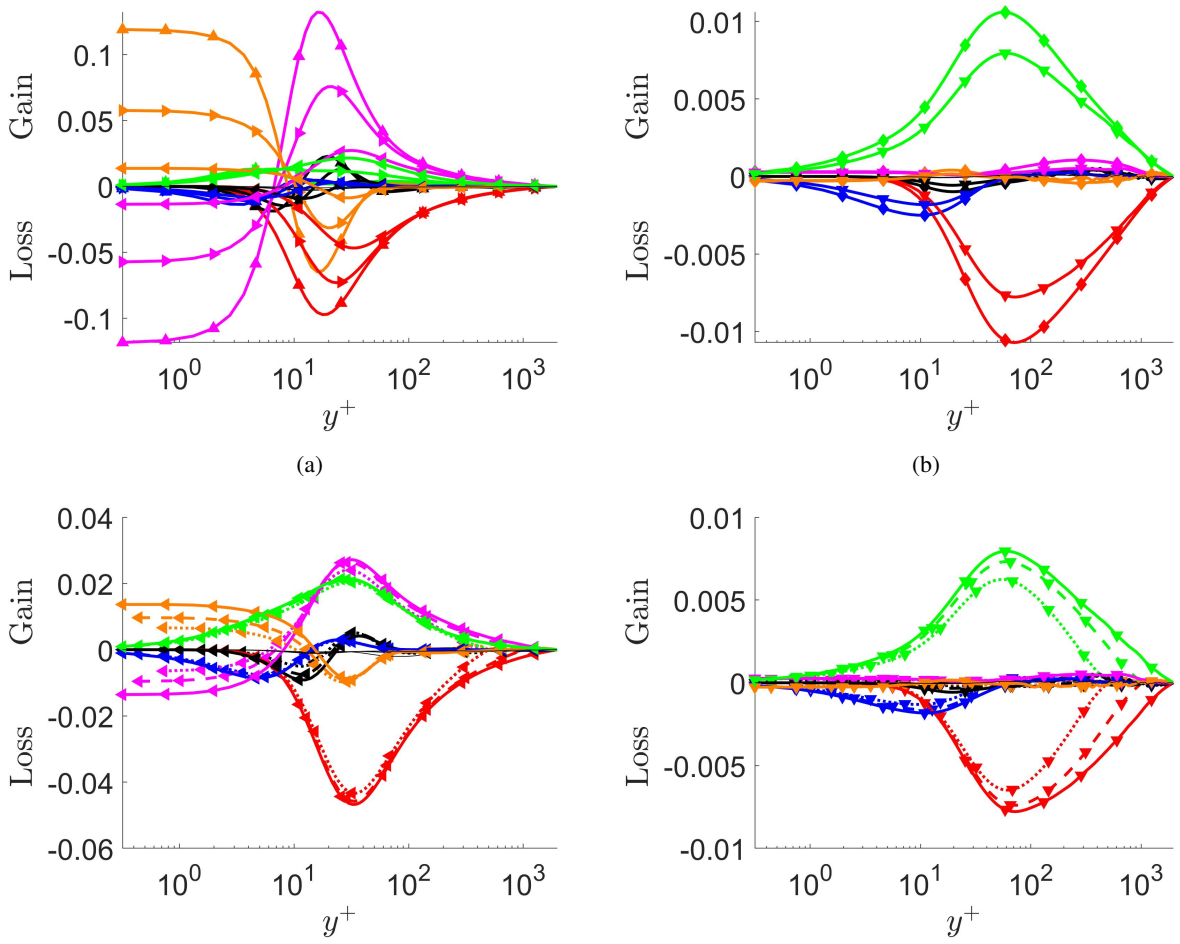

Figure 11: Colour online. Budgets of the wall-normal heat flux, $\overline{v\theta}$, for $Re_\tau = 2000$ and (a) medium Prandtl numbers: $Pr = 0.71$, 0.3 and 0.1; (b) low Prandtl numbers: $Pr = 0.01$ and 0.007. $Re_\tau = 2000$, 1000 and 500 for (c) $Pr = 0.1$ and (d) $Pr = 0.007$. Colours here denote budget terms: production (red), turbulent diffusion (black), viscous diffusion (blue), dissipation (green), pressure-temperature-gradient correlation (magenta) and pressure diffusion (orange). Line style determines the Re_τ number: $Re_\tau = 2000$ (solid line), $Re_\tau = 1000$ (dashed line) and $Re_\tau = 500$ (pointed line). Symbols as in Table 2.

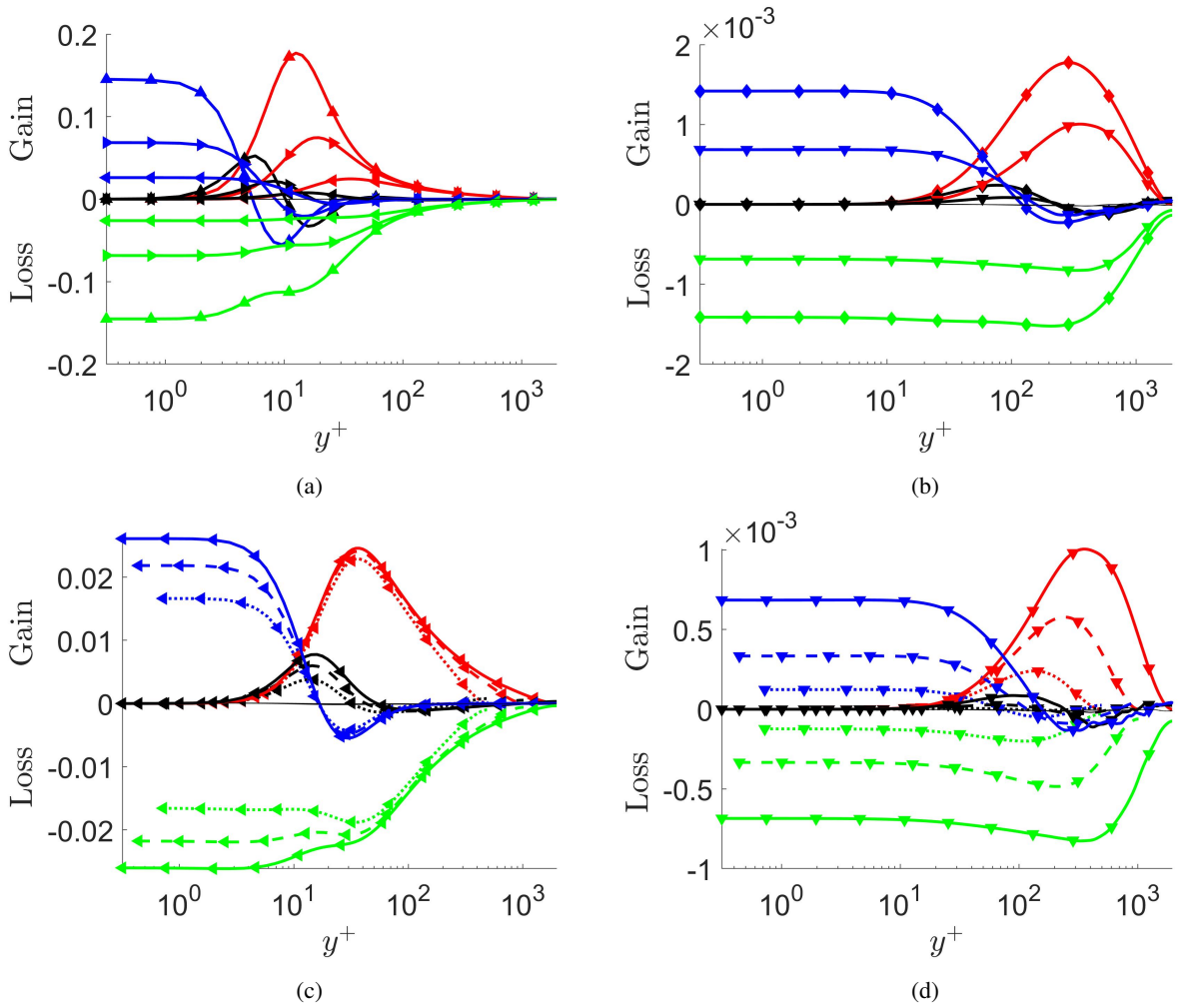

Figure 12: Colour online. Budgets of the temperature variance, $\overline{k_\theta}$, for $Re_\tau = 2000$ and (a) medium Prandtl numbers: $Pr = 0.71$, 0.3 and 0.1; (b) low Prandtl numbers: $Pr = 0.01$ and 0.007. $Re_\tau = 2000$, 1000 and 500 for (c) $Pr = 0.1$ and (d) $Pr = 0.007$. Colours here denote budget terms: production (red), turbulent diffusion (black), viscous diffusion (blue) and dissipation (green). Line style determines the Re_τ number: $Re_\tau = 2000$ (solid line), $Re_\tau = 1000$ (dashed line) and $Re_\tau = 500$ (pointed line). Symbols as in Table 2.

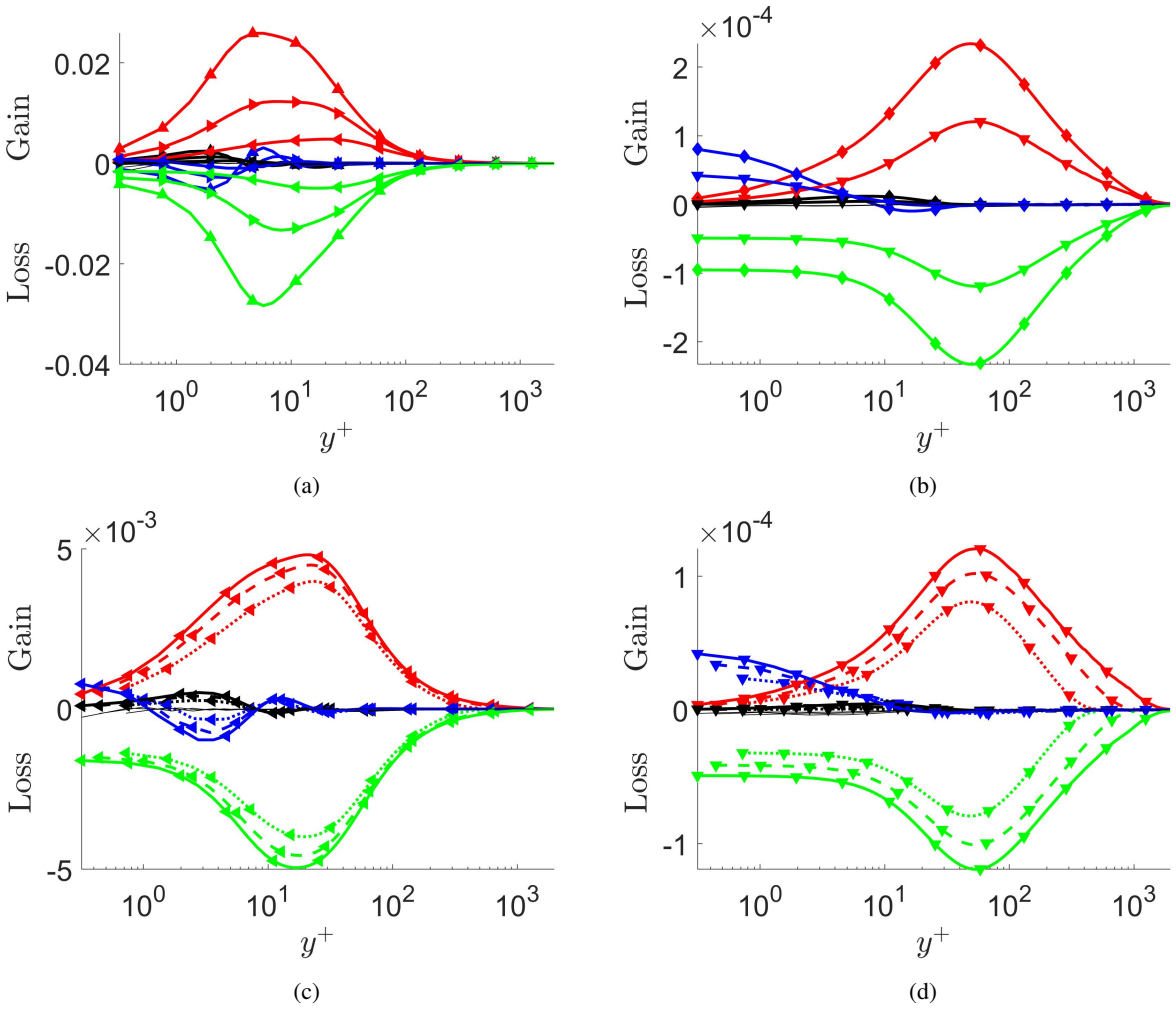

Figure 13: Colour online. Budgets of the dissipation rate of the temperature variance, $\overline{\varepsilon_\theta}$, for $Re_\tau = 2000$ and (a) medium Prandtl numbers: $Pr = 0.71$, 0.3 and 0.1; (b) low Prandtl numbers: $Pr = 0.01$ and 0.007. $Re_\tau = 2000$, 1000 and 500 for (c) $Pr = 0.1$ and (d) $Pr = 0.007$. Mixed production, mean gradient production, gradient production and turbulent production have been added and plotted as an only production term. Colours here denote budget terms: added production (red), turbulent diffusion (black), viscous diffusion (blue) and dissipation (green). Line style determines the Re_τ number: $Re_\tau = 2000$ (solid line), $Re_\tau = 1000$ (dashed line) and $Re_\tau = 500$ (pointed line). Symbols as in Table 2.

5. Conclusions

A new set of Direct Numerical Simulations of turbulent heat transfer in a channel flow are presented. Uniform heating from both walls is used as the boundary condition. The effects in the thermal flow of Re_τ and medium to low molecular Prandtl numbers is study for a range of values of: Re_τ = 500, 1000 and 2000; and $Pr = 0.007 - 0.71$.

A balance of the heat fluxes is calculated to validate the simulations. It is seen that when Pr is reduced, molecular heat flux becomes more important than turbulent heat flux. Indeed, for the lowest Prandtl number, turbulent heat flux is almost negligible except in the central region of the channel.

First, instantaneuos visualizations of the flow have been examined. For Prandtl numbers close to 1, $Pe_\tau \sim Re_\tau$ and, therefore, turbulent scales of the velocity field and thermal field are of the same order of magnitude. However, when Pr is reduced, the thermal field becomes less turbulent and turbulent length scales increase.

Mean temperature profiles, the diagnosis function and turbulent intensities (θ'^+, $\overline{u^+\theta^+}$ and $\overline{v^+\theta^+}$) are shown. The logarithmic region appears only for Prandtl numbers greater than approximately 0.3. The von Kármán constant is calculated and it seems to be, indeed, constant for $Re_\tau >= 1000$, with value 0.43. The values of the diagnosis function in the central region of the channel collapse for $Pe_\tau > 30$. On the other hand, the morphology of the turbulent intensities change when $Pr > 0.3$. Also, in the outer region, their values collapse when the Péclet number is greater than 325 for θ'^+ and $\overline{u^+\theta^+}$; and 225 for $\overline{v^+\theta^+}$. In addition, the location of the maximua of the functions does not depend on the Reynolds number when the maximum is located in the buffer layer or in the logarithmic region. However, for lower Prandtl numbers, the maxima location moves to the outer region and it does depend on the Reynolds number. The absolute values of all three intensities decrease when Pr is reduced, which means that, in fact, the thermal flow is less turbulent.

The Nusselt number is derived from the mean temperature profile. It is seen that it can be represented with a linear logarithmic expression for medium-low to medium Prandtl numbers. This range seems to increase, at least the lower limit of Pr, when Re_τ is increased. However, the upper limit of the linear behaviour is not captured in this work, since it is greater than 0.71. Another dimensionless number calculated is the turbulent Prandtl number. As it was known, for $Pr > 0.05$, its value is more or less constant and approximately 1 in all the channel. For $Pr <= 0.05$, the turbulent Prandtl number increases as the molecular Prandtl or Re_τ decrease.

A comparison with the results from [18] for the simulations of higher Reynolds and a value of Prandtl of $Pr = 0.71$ have been done. For that work a boundary condition different to the MBC and similar to the one used in [7] was used. Results are not exactly the same but similar. Also, tendencies of the thermal variables are the same. Thermal values tend to increase when the MBC is used, especially in the central region of the channel.

Finally, turbulent budgets for heat fluxes, temperature variances and its dissipation rate are presented. For $\overline{v\theta}$, the pressure terms become negligible when Pr is reduced, and dissipation compensates the production term. As it was expected, turbulent diffusion is negligible for all low Prandtl number cases. Also, scaling laws are analyzed. It is seen that for low Prandtl numbers, any of them work properly and a deeper study is needed. The most conflictive terms, especially in the near wall region, are dissipation and viscous diffusion, pressure terms for $\overline{v\theta}$ and production for $\overline{\varepsilon_\theta}$.

As a final remark, any scaling law for both the intensities and turbulent budgets should consider the Pr and Re_τ dependencies. To unveil these scaling laws, a Lie-Symmetry framework, as in [32], is being used by the authors. Also, simulations at higher Prandtl are needed to get a global picture of the situation. These simulations would be harder, as the heat equation has to be properly solved and a finer mesh would be needed. Finally, to help other researchers to test their theories, the statistics of all simulations can be downloaded from the web page of our `group`.

6. Acknowledgments

This work was supported by MINECO/FEDER, under project ENE2015-71333-R. The computations of the new simulations were made possible by a generous grant of computing time from the Barcelona Supercomputing Centre, reference FI-2018-1-0037. We are grateful to Messiers Kawamura, Pirozzoli, Bernardini and Orlandi for providing us with copies of their original data.

References

[1] J. Slotnick, A. Khodadoust, J. Alonso, D. Darmofal, W. Gropp, E. Lurie, and D. Mavriplis. Cfd vision 2030 study: A path to revolutionary computational aerosciences. *NASA TECHNICAL REPORT*, (218178), 2014.

[2] A. Browb and B. W. Martin. A review of the bases of predicting heat transfer to gas turbine rotor blades. *The American Society of Mechanical Engineers*, 1A, 1974.

[3] D. K. Tafti, L. He, and K. Nagendra. Large eddy simulation for predicting turbulent heat transfer in gas turbines. *Philosophical Transactions of the Royal Society A: Mathematical, Physical and Engineering Sciences*, 372(2022), 2014.

[4] G. Grötzbach. Challenges in low-prandtl number heat transfer simulation and modelling. *Nuclear Engineering and Design*, 264:41–55, 2013.

[5] M. Duponcheel, L. Bricteux, M. Manconi, G. Winckelmans, and Y. Bartosiewicz. Assessment of rans and improved near-wall modeling for forced convection at low prandtl numbers based on les up to $Re_\tau = 2000$. *International Journal of Heat and Mass Transfer*, 75:470–482, 2014.

[6] H. Cachafeiro, L. Fdez. de Arevalo, R. Vinuesa, J. Goikoetxea, and J. Barriga. Impact of solar selective coating ageing on energy cost. *Energy Procedia*, 69:299–309, 2015.

[7] John Kim and Parviz Moin. Transport of passive scalars in a turbulent channel flow. *NASA*, 1(TM-89463):1–14, 1987.

[8] S.L. Lyons, T.J. Hanratty, and J.B. McLaughlin. Direct numerical simulation of passive heat transfer in a turbulent channel flow. *International Journal of Heat and Mass Transfer*, 34(4-5):1149–1161, 1991. cited By 100.

[9] N Kasagi, Y Tomita, and A Kuroda. Direct numerical simulation of passive scalar field in a turbulent channel flow. *Journal of Heat Transfer*, 114(3):598–606, August 1992.

[10] M. Piller. Direct numerical simulation of turbulent forced convection in a pipe. *International Journal for Numerical Methods in Fluids*, 49:583–602, 2005.

[11] T. Yano and N Kasagi. Direct numerical simulation of turbulent heat transport at high prandtl numbers. *JSME International Journal, Series B: Fluids and Thermal Engineering*, 42(2):284–292, 1999.

[12] Hiroshi Kawamura, Kouichi Ohsaka, Hiroyuki Abe, and Kiyoshi Yamamoto. DNS of turbulent heat transfer in channel flow with low to medium-high Prandtl number fluid. *International Journal of Heat and Fluid Flow*, 19(5):482–491, 1998.

[13] Hiroshi Kawamura, Hiroyuki Abe, and Yuichi Matsuo. DNS of turbulent heat transfer in channel flow with respect to Reynolds and Prandtl number effects. *International Journal of Heat and Fluid Flow*, 20:196–207, 1999.

[14] Hiroyuki Abe, Hiroshi Kawamura, and Yuichi Matsuo. Surface heat-flux fluctuations in a turbulent channel flow up to $Re_\tau = 1020$ with $Pr = 0.025$ and 0.71. *International Journal of Heat and Fluid Flow*, 25(3):404–419, 2004.

[15] Yohji Seki and Hiroshi Kawamura. DNS of turbulent heat transfer in channel flow with a varying streamwisely thermal boundary condition. *Heat transfer – Asian Research*, 35(4):265–278, 2006.

[16] A. Lozano-Durán and J. Jiménez. Effect of the computational domain on direct simulations of turbulent channels up to $Re_\tau = 4200$. *Physics of Fluids*, 26(1):011702, 2014.

[17] F. Lluesma-Rodríguez, S. Hoyas, and MJ Peréz-Quiles. Influence of the computational domain on dns of turbulent heat transfer up to $Re_\tau = 2000$ for $Pr = 0.71$. *International Journal of Heat and Mass Transfer*, 122:983–992, 2018.

[18] S. Pirozzoli, M. Bernardini, and P. Orlandi. Passive scalars in turbulent channel flow at high reynolds number. *Journal of Fluid Mechanics*, 788:614–639, 2016.

[19] S. K. Lele. Compact finite difference schemes with spectral-like resolution. *Journal of Computational Physics*, 103(1):16–42, 1992.

[20] Philippe R Spalart, Robert D Moser, and Michael M Rogers. Spectral methods for the Navier-Stokes equations with one infinite and two periodic directions. *Journal of Computational Physics*, 96(2):297–324, 1991.

[21] Sergio Hoyas and Javier Jiménez. Scaling of the velocity fluctuations in turbulent channels up to $Re_\tau = 2003$. *Physics of Fluids*, 18(1):011702, 2006.

[22] V. Avsarkisov, S. Hoyas, M. Oberlack, and J.P. García-Galache. Turbulent plane Couette flow at moderately high reynolds number. *Journal of Fluid Mechanics*, 751:R1, 2014.

[23] S. Hoyas and J. Jiménez. Reynolds number effects on the Reynolds-stress budgets in turbulent channels. *Physics of Fluids*, 20(10):101511, 2008.

[24] Sergio Ganda-Barber, Sergio Hoyas, Martin Oberlack, and Stefanie Kraheberger. The link between the reynolds shear stress and the large structures of turbulent couette-poiseuille flow. *Physics of Fluids*, 30(4):041702, 2018.

[25] R. Vinuesa, C. Prus, P. Schlatter, and H.M. Nagib. Convergence of numerical simulations of turbulent wall-bounded flows and mean cross-flow structure of rectangular ducts. *Meccanica*, 51(12):3025–3042, 2016.

[26] J. Jiménez. Near-wall turbulence. *Physics of Fluids*, 25(10):101302, 2013.

[27] M. Lee and R. Moser. Direct numerical simulation of turbulent channel flow up to $Re_\tau \approx 5200$. *Journal of Fluid Mechanics*, 774:395–415, 2015.

[28] M. Bernardini, S. Pirozzoli, and P. Orlandi. Velocity statistics in turbulent channel flow up to $Re_\tau = 4000$. *Journal of Fluid Mechanics*, 758:327343, 2014.

[29] S. Kraheberger, S. Hoyas, and M. Oberlack. Dns of a turbulent couette flow at constant wall transpiration up to $Re_\tau = 1000$. *Journal of Fluid Mechanics*, 835:421–443, 2018. cited By 0.

[30] Y. Sumitani and N. Kasagi. Direct numerical simulation of turbulent transport with uniform wall injection and suction. *AIAA Journal*, 33:1220–1228, 1995.

[31] Makoto Kozuka, Yohji Seki, and Hiroshi Kawamura. DNS of turbulent heat transfer in a channel flow with a high spatial resolution. *International Journal of Heat and Fluid Flow*, 30(3):514–524, 2009.

[32] V. Avsarkisov, M. Oberlack, and S. Hoyas. New scaling laws for turbulent Poiseuille flow with wall transpiration. *Journal of Fluid Mechanics*, 746:99–122, 2014.